AGU PUBLICATIONS

JGR

Journal of Geophysical Research: Atmospheres

RESEARCH ARTICLE
10.1002/2016JD026099

Key Points:
- Development of a new diagnostic of soil moisture bimodality
- Soil moisture bimodality larger in transitional climates and high latitudes
- CMIP5 climate models show distinctive higher values of soil moisture bimodality

Supporting Information:
- Supporting Information S1

Correspondence to:
L. Vilasa,
luis.vilasa@gmail.com

Citation:
Vilasa, L., D. G. Miralles, R. A. M. de Jeu, and A. J. Dolman (2017), Global soil moisture bimodality in satellite observations and climate models, *J. Geophys. Res. Atmos.*, *122*, 4299–4311, doi:10.1002/2016JD026099.

Received 27 DEC 2016
Accepted 4 APR 2017
Accepted article online 7 APR 2017
Published online 27 APR 2017

Global soil moisture bimodality in satellite observations and climate models

L. Vilasa[1], D. G. Miralles[1,2], R. A. M. de Jeu[1,3], and A. J. Dolman[1]

[1]Department of Earth Sciences, VU University Amsterdam, Amsterdam, Netherlands, [2]Laboratory of Hydrology and Water Management, Ghent University, Ghent, Belgium, [3]VanderSat B.V., Haarlem, Netherlands

Abstract A new diagnostic metric based on soil moisture bimodality is developed in order to examine and compare soil moisture from satellite observations and Earth System Models. The methodology to derive this diagnostic is based on maximum likelihood estimator encoded into an iterative algorithm, which is applied to the soil moisture probability density function. This metric is applied to satellite data from the Advanced Microwave Scanning Radiometer for the Earth Observing System and global climate models data from the Coupled Model Intercomparison Project Phase 5 (CMIP5). Results show high soil moisture bimodality in transitional climate areas and high latitudes, potentially associated with land-atmosphere feedback processes. When comparing satellite versus climate models, a clear difference in their soil moisture bimodality is observed, with systematically higher values in the case of CMIP5 models. These differences appear related to areas where land-atmospheric feedback may be overestimated in current climate models.

1. Introduction

Surface soil moisture is a diagnostic of the impact of climate on land conditions and is crucial for hydrological modeling, agricultural management, and flood forecasting. It also plays a prominent role in climate variability due to its control on the surface energy balance [*Entekhabi et al.*, 1999]. Soil moisture affects both average temperature and precipitation at climatological scales [*Seneviratne et al.*, 2010; *Koster et al.*, 2004] as well as the occurrence of hydroclimatic extremes [*Teuling et al.*, 2010; *Miralles et al.*, 2014]. Simulations from climate and weather forecast models have demonstrated the impact of soil moisture on the atmosphere at different spatiotemporal scales [*Koster et al.*, 2006; *van den Hurk et al.*, 2012]. In addition, recent efforts have detected the influence of soil moisture on climate variability by using satellite [*Miralles et al.*, 2012; *Mueller and Seneviratne*, 2012; *Taylor et al.*, 2012] and in situ observations [*Hirschi et al.*, 2011; *Tuttle and Salvucci*, 2016]. These studies pointed to the need of representing soil moisture feedback adequately in climate models in order to reduce the uncertainty in their projections of future temperature and precipitation [*Seneviratne et al.*, 2010] and highlighted the misrepresentation of these interactions by current models [*Taylor et al.*, 2012].

During the last decades, a wide range of global soil moisture data sets have been developed which can be used for the purpose of investigating the realism of soil moisture–atmosphere interactions in climate models. These data sets include land surface models driven by observations [*Bolten et al.*, 2010; *Albergel et al.*, 2012; *Miralles et al.*, 2011], atmospheric reanalysis [*Balsamo et al.*, 2012; *Reichle et al.*, 2011], and satellite-based products [*Owe et al.*, 2008; *Bartalis et al.*, 2007; *Kerr et al.*, 2012]. Here we diagnose the realism of the soil moisture simulated by the climate models from the Coupled Model Intercomparison Project Phase 5 (CMIP5) by analyzing their soil moisture bimodality based on a new metric. We refer to soil moisture bimodality when the soil moisture data probability density function has the shape of a bimodal distribution, that is a continuous probability distribution with two different modes that may appear as distinct peaks.

Among the processes that may trigger soil moisture bimodality, we can find the simple climatic seasonality, with the two preferential soil moisture states centered around the mean values for the wet and dry seasons [*Teuling et al.*, 2005]. We can also find ocean-atmospheric oscillations, such as El Niño–Southern Oscillation, acting at multiyear time scales [*Poveda et al.*, 2001], and processes like the monsoons or high-latitude freeze-thaw cycles causing bimodality at subseasonal scales [*Douville et al.*, 2006]. In addition, experimental studies have suggested that the interplay between the saturated and the unsaturated zone may also induce soil moisture bimodality [*Daly et al.*, 2009]. In the time scale range of several weeks, other less obvious processes can cause bimodality as well, including land-atmosphere feedback or the offset of the monsoon.

Some authors have hypothesized that soil moisture bimodality is linked to preferential dry/wet states in the soil moisture caused by positive soil moisture-precipitation feedback [*D'Odorico et al.*, 2000; *D'Odorico and Porporato*, 2004], although other studies have indicated that the combination of seasonality with the nonlinearity of the soil moisture response to climate is enough to create this bimodal behavior [*Teuling et al.*, 2005].

A variety of land-atmospheric interactions (including both impacts of climate on soil moisture as well as feedback from soil moisture on climate) can cause the soil moisture probability density function to present a bimodal distribution. This gives us the opportunity to jointly assess different properties of the spatiotemporal soil moisture variability that should be correctly represented by climate models. Therefore, the spatiotemporal assessment of soil moisture bimodality implies an alternative to more traditional evaluations and enables the evaluation of statistical properties of soil moisture that appear critical for land-atmospheric interactions. While our diagnostic may in principle be applied to any climatic or environmental variable, in the present study it is used to evaluate the realism of the CMIP5 simulations of soil moisture by benchmarking them against global satellite retrievals. In the following, we describe the derivation of the bimodality metric (sections 2 and 3) and analyze the discrepancies between models and observations with regard to soil moisture bimodality (section 4).

2. Data

We are interested in knowing the spatial distribution and persistence of soil moisture bimodality and exploring the differences in its representation in global climate models (GCMs) and observational data sets. Therefore, our methodology requires consistent and long records of satellite and model outputs. We selected the satellite-derived soil moisture data set based on the Advanced Microwave Scanning Radiometer–EOS (AMSR-E) sensor and an algorithm developed based on *Owe et al.* [2008]. The AMSR-E data set was chosen due to its multiyear record (June 2002 to October 2011), single-sensor nature, and global coverage; these are necessary conditions to meet the previously stated requirements. This satellite soil moisture data set was derived from low-frequency (C and X bands) brightness temperature observations and obtained by using the Land Parameter Retrieval Model (LPRM) to convert these observations into soil moisture values for the first few centimeters of soil [*Owe et al.*, 2008]. Data are available in a 0.25×0.25 grid, with near-global coverage twice per day, corresponding with the satellite ascending and descending overpasses. A screening of unreliable observations was performed by removing the 15% of observations with higher errors, based on the analytical error propagation model by *Parinussa et al.* [2011].

We also use the outputs from the CMIP5 experiment [see, e.g., *Taylor et al.*, 2011], in particular those from its sister Atmospheric Model Intercomparison Project (AMIP), now fully integrated within CMIP [*Gates*, 1992]. The AMIP experiment has a simple design: atmospheric global circulation models are constrained by realistic sea surface temperature and sea ice from 1979 to near present [*Taylor et al.*, 2011]; thus, these boundary conditions are shared by all models included in this study. These configuration choices enable researchers to focus on the atmosphere and land parts of the climate system without the added complexity of ocean-atmosphere feedback. From the AMIP set of simulations, we select models that provide daily soil moisture data. The complete list of models employed and additional information about them can be found in Table S1 in the supporting information [*Collins et al.*, 2011; *Essery and Clark*, 2003; *Hirai et al.*, 2007; *Mizuta et al.*, 2012; *Noilhan and Mahfouf*, 1996; *Oleson et al.*, 2004; *Quandt and Ramsey*, 1978; *Rosenzweig and Abramopoulos*, 1997; *Schmidt et al.*, 2006; *Takata et al.*, 2003; *Verseghy*, 2000; *Voldoire et al.*, 2013; *Volodin et al.*, 2010; *Volodin and Lykosov*, 1998; *von Salzen et al.*, 2013; *Watanabe et al.*, 2011; *Wu et al.*, 2010; *Yukimoto et al.*, 2012].

The model variable analyzed (named "mrsos" in the CMIP5 archives, short for "Moisture in upper portion of soil column") is the integral value over the uppermost 10 cm of the soil column of the mass of water in all phases in that layer. AMSR-E satellite soil moisture data are obtained from a layer of heterogeneous depth comprising the first few centimeters. This could potentially lead to discrepancies between models and observations, although given the time scale of our analysis, these differences in representative depth are here assumed not to play a critical role. All data sets used for our analysis are preprocessed in the same way in order to create consistent data samples: for each grid cell, we collect soil moisture data from a 2 month moving window from every year. The periods used for this analysis are 2002–2011 for the AMSR-E observations and 2000–2008/2009 for the CMIP5 climate models. Our statistical analysis is independently applied to this sample of data points.

3. Methodology

To validate and intercompare soil moisture data sets, standard metrics (such as correlation coefficients, root-mean square-errors, and bias) and more elaborate methods [see, e.g., *Crow and Van Den Berg*, 2010; *Scipal et al.*, 2008] have been applied in the past. These metrics may be used to investigate the quality of soil moisture simulations in GCMs; however, they do not necessarily yield information on the properties of soil moisture that truly determine its interplay with the atmosphere. Evaluating the spatiotemporal variability of soil moisture bimodality implies therefore an alternative to more traditional metrics and enables the assessment of statistical properties of the soil moisture that appear critical for land-atmospheric studies and that should also be captured by current climate models. Our statistical framework to detect bimodality is illustrated in Figure 1 and could be summarized as follows: (1) gathering of the data for the selected time period (section 2), (2) calculation of the likelihood of a Gaussian distribution and the fit and likelihood of a two-mode Gaussian mixture model (GMM) (section 3.1), and (3) determination of the bimodality at each grid cell (section 3.2). In the following subsections, we present a detailed explanation of these main steps.

3.1. Data Fit

Our framework assumes that the probability density function (PDF) of a soil moisture time series can be described either by one Gaussian distribution (i.e., unimodal) or by a two-mode (i.e., bimodal) GMM. Therefore, the presence of unimodal or bimodal distributions in the soil moisture PDF is tested by fitting the data to both a simple Gaussian distribution and a GMM. A GMM is a parametric PDF model constructed from a weighted sum of individual Gaussian PDF components. The probability distributions of continuous measurements are commonly parameterized as GMMs. In our particular case, we use a GMM composed by two densities, whose weights, means, and standard deviations are the parameters adjusted by using the expectation-maximization (EM) algorithm, and we use the likelihood function to determine and quantify the goodness of each fit.

We perform the analysis for the AMSR-E and CMIP5 global data set grids on a pixel-by-pixel basis; i.e., each grid cell is treated independently. For each grid cell, we collect soil moisture data for a selected 2 month time window from every year available in the data sets. Our statistical analysis is applied to this sample of data points. Sensitivity tests are performed to make a balanced choice for the length of the time window. The 2 month window has been chosen for being the minimum time window size one can choose with the length of the selected data sets in order to have enough data points to derive a reliable histogram.

The core of our analysis is the expectation-maximization (EM) algorithm. It is assumed that the probability density function (PDF) of a soil moisture sample can be described either by one Gaussian distribution (i.e., unimodal) or by a two-mode (i.e., bimodal) Gaussian mixture model (GMM). Therefore, the presence of unimodal or bimodal distributions in the soil moisture PDF is tested by fitting the data to a Gaussian distribution and a GMM with EM algorithm. The results of the test are filtered by dependent and independent additional tests of bimodality based on the relations between the GMM parameters; these tests act as unimodal/bimodal masks and allow us to define bimodality areas. Once the analysis is finished for each grid point, we can build global maps showing the analysis' results, wherein the grouping of points shows bimodality areas of interest.

3.1.1. Gaussian Mixture Models

A GMM is a parametric PDF model constructed from a weighted sum of individual Gaussian PDF components. The probability distributions of continuous measurements are commonly parameterized as GMMs. We use a GMM as the base PDF, and we find the values of its parameters that fit best to our data samples. The general formulation for a GMM is as follows:

$$P(x|\lambda) = \sum_{i=1}^{M} \omega_i g\left(x|\mu_j, \Sigma_j\right) \tag{1}$$

where x is a vector of continuous random data(sample), $\omega_i, i = j,...,K$, are the mixture weights, and $g(x|\mu_j, \Sigma_j)$, $j = 1,...,K$, are the component Gaussian densities, being K the number of modes. Each component density is a Gaussian function of the form

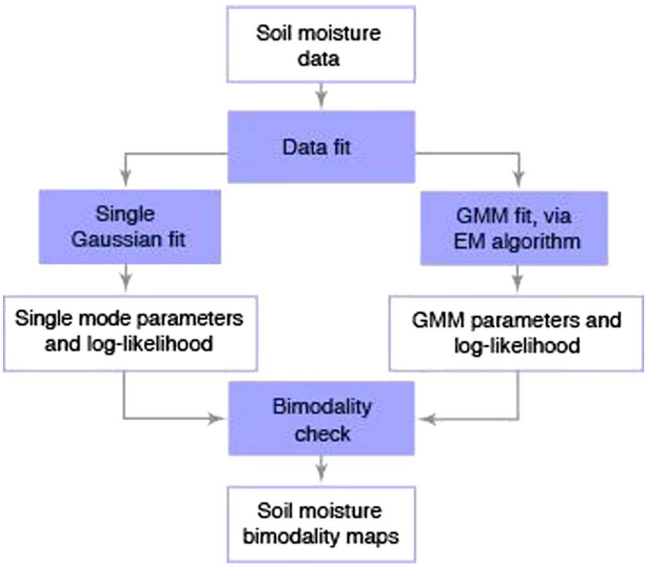

Figure 1. Flowchart for the bimodality detection framework. The data fit and bimodality check are explained in sections 3.1 and 3.2, respectively.

$$g\left(x|\mu_j,\Sigma_j\right)=\frac{1}{\left|(2\pi)^{\frac{D}{2}}\left|\Sigma_j\right|^{\frac{1}{2}}\right|}\exp\left(-\left(x-\mu_j\right)\Sigma_j\left(x-\mu_j\right)\right) \tag{2}$$

with vector of means μ_j and covariance matrix Σ_j.

The covariance matrices of the different components, Σ_j, can be full rank or constrained to be diagonal. The mixture weights satisfy the following constraint:

$$\sum_{i=j}^{K}\omega_j=1 \tag{3}$$

The complete set of parameters for a particular GMM includes the mean vectors, covariance matrices, and mixture weights for each of its component densities. In our particular case, we use a GMM composed by two component densities; the remaining parameters, components weight, mean vector, and covariance matrices are adjusted during our analysis. Since our object of study, soil moisture, is a scalar variable, mean vectors and covariance matrices will be reduced to single-scalar values.

3.1.2. Log Likelihood

The likelihood function is a function of the parameters of a statistical model, in the case of a GMM fitted to a sample, and is equal to the probability of the observed data given the particular parameters of the GMM. Here we try to find the GMM parameters that maximize the likelihood function.

The likelihood function for a GMM with a set of parameters (λ), being x is a vector of continuous random data (sample), can be expressed as follows:

$$L(\lambda|x)=P(x|\lambda)=\prod_{i=1}^{N}P(x_i|\lambda)=\prod_{i=1}^{N}\sum_{j=1}^{K}P\left(x_i|\omega_j,g_j\right)P\left(\omega_j\right) \tag{4}$$

A derivation from the likelihood function is the log likelihood function. The natural logarithm is a monotonically increasing function, which makes both likelihood and log likelihood expressions equivalent for our goals, and since the resulting expression is more convenient for encoding, we can take the log likelihood (l) as

$$l(\lambda|x)=\log L(\lambda|x)\ =\sum_{i=1}^{N}P(x_i|\lambda)=\sum_{i=1}^{N}\sum_{j=1}^{K}P\left(x_i|\omega_j,g_j\right)P\left(\omega_j\right) \tag{5}$$

where ω_k are the weights associated to each of the GMM modes and g_k are the probability density function of each one of the individual modes.

3.1.3. Expectation-Maximization Algorithm

The expectation-maximization (EM) algorithm is an iterative method that attempts to find the maximum likelihood estimator of a set of parameters from a parametric probability distribution [*Gupta and Chen*, 2010].

The key elements in the formulation of the EM algorithm are (1) a description of the phenomenon (complete data), which we assume can be modeled as a continuous random vector Y with a parametric PDF $P(y|\lambda)$, where $\lambda \in \Omega$ for some set Ω, and (2) a measure or realization of this phenomenon, our observed data X, with a parametric PDF $P(x|\lambda)$. In our case, for a GMM, the X vector is composed by our data and the complete data Y is the composition of our data plus the information about to which of the modes pertain each of the data points.

The objective of the process is to find the maximum likelihood estimate (MLE) of the set of parameters λ, which can be done easily in simple cases by calculating the λ that maximizes $P(x|\lambda)$: $\lambda^{\mathrm{MLE}} = \mathrm{argmax}[\lambda\ P(x|\lambda)]$, $\lambda \in \Omega$. For more complex $P(x|\lambda)$, the use of alternative methods, like the EM algorithm, is advised [*Gupta and Chen*, 2010]. As previously stated, since the logarithm is a monotonically increasing function, the expressions of the likelihood and log likelihood are equivalent for maximization purposes, which allows us to use the more convenient log likelihood expression in our calculations.

The EM makes a guess about the complete data Y and then finds a solution for the λ that maximizes the expected log likelihood of Y. Once we have an estimation of the set of parameters λ, we can make a better guess about the complete data and start iterating from there.

EM is usually described as two-step process: The expectation step (E step) and the maximization step (M step). Based on *Gupta and Chen* [2010], we can describe the EM algorithm in the following steps:

1. Initialization: Let $m = 0$ (first step) and make an initial estimate for λ, for our particular case: two modes ($k = 2$) in a one-dimensional space, $\lambda(0) = \omega_{j0}, \mu_{j0}, \sigma_{j0}, j = 1, 2$.
2. E step: Given the observed data y and pretending for the moment that your current guess $\lambda(m)$ is correct, formulate the conditional probability distribution $P(y|x,\lambda(m))$ for the complete data y. Using the conditional probability distribution $P(y|x,\lambda(m))$ form the conditional expected log likelihood, which is called the Q function:

$$Q(\lambda|\lambda(m)) = Y(x)\int_{Y(x)} \log P(y|\lambda)P(y|x,\lambda(m)) = E_{Y|x,\lambda(m)}[\log P(Y|\lambda)] \tag{6}$$

   where the integral is over the set Y (x), which is the closure of the set y $P(y|x,\lambda) > 0$, and we assume that Y (x) does not depend on λ. The construction of the Q function is the key point of this step. Note that λ is a free variable in the expression of the Q function, so the Q function is a function of λ but also depends on your current guess $\lambda(m)$ implicitly through the $P(y|x,\lambda(m))$ function calculated in this step. In our case the Q function has the following shape:

$$Q(\lambda|\lambda(m)) = \sum_{i=1}^{N}\sum_{j=1}^{K} \gamma_{ij}^{m}\left(\log\omega_j - \log\sigma_j - \frac{x_i - \mu_j}{2\sigma^2}\right) \tag{7}$$

   being γ_{ij} the estimate at the mth iteration of the probability that the ith sample was generated by the jth Gaussian component:

$$\gamma_{ij}^{m} = \frac{\omega_j^m g\left(x_i|\mu_j,\sigma_j\right)}{\omega_1^m g(x_i|\mu_1,\sigma_1) + \omega_2^m g(x_i|\mu_2,\sigma_2)} \tag{8}$$

   Although since our only interest in construction of the Q function is in its maximization and the posterior construction of a new estimate in the M step, following the work of *Gupta and Chen* [2010], in this step we only need to calculate the parts of the Q function that depend on λ, the γ_{ij} estimate, and the membership weight of the jth Gaussian, which will also be used in the next step and can be defined as

$$n_j^m = \sum_{i=1}^{N} \gamma_{ij}^{m} \tag{9}$$

3. M step: Find the λ that maximizes the Q function; the result is the new estimate $\lambda(m+1)$. The computation of the new estimates is reduced to

$$\omega_j^{m+1} = \frac{n_j^m}{n} \tag{10}$$

$$\mu_j^{m+1} = \frac{\sum_{i=1}^{N} \gamma_{ij}^m x_i}{n_j^m} \tag{11}$$

$$\sigma_j^{m+1} = \sqrt{\left(\frac{1}{n_j^m} \sum_{i=1}^{N} \gamma_{ij}^m \left(x_i - \mu_j\right)^2\right)} \tag{12}$$

4. Convergence check: If the convergence check is not met, let $m = m + 1$ and go back to E step. There is no convergence check specified in the formulation of the EM algorithm; the standard stopping criteria is to iterate until the estimate (λ) or the log likelihood $l(\lambda) = \log P(x|\lambda)$ stops changing; in our case, we choose to monitor the log likelihood evolution:

$$\epsilon > |l(m+1) - l(m)| > 0 \tag{13}$$

being ϵ a constant greater than 0.

The EM estimate evolves from the starting point and is guaranteed to never worsen. If the likelihood function $P(x|\lambda)$ has more than two peaks (statistical aberration or any kind of systemic error can generate an additional peak), there is the risk for the EM algorithm not finding the global maximum, and stopping at a relative maximum, therefore incorrectly detecting the potential modes. This risk can be greatly reduced with a careful selection of the analysis' starting point [*Gupta and Chen*, 2010].

As the proposed GMM has always more adjustable parameters, it will always fit better than the single Gaussian distribution. For this reason, we have to develop a method to quantify the relative improvement of the fit. In the absence of a definitive indicator, we designed a sorting strategy based on several different approximate measures and necessary conditions for bimodality. We will later use these indicators as masks to achieve our definitive results.

3.2. Bimodality Check

The first goal after our analysis is the definition of high bimodality areas. In order to do so, we could think of using the difference between the log likelihood of the single-mode and the two-mode models, but this is impractical for several reasons related to the limitations of our analysis. We made the assumption that the soil moisture is a Gaussian process, and as such, its character should appear in the probability density of our data of study. Several circumstances can concur, limiting the progress of our analytical techniques, for example, soil moisture not showing a Gaussian nature, noise, and limited data availability.

In order to compensate for these limitations, and in order to be able to advance toward our goals, we use several additional tests of bimodality based on the relations between the GMM parameters; these tests act as unimodal/bimodal masks and allow us to define bimodality areas. Some of them are derived from our a priori knowledge of the subject of study; some others are purely mathematical tests. These discrimination mechanisms—in conjunction with the original log likelihood result—allow us to create bimodality maps. We will thus set a threshold of minimum ratio between modes' standard deviations and a minimum ratio between modes' weights. Previous literature also gives a minimum threshold for Ashman's D statistic, which establishes a weighted minimum difference between modes means. This is also applied.

3.2.1. Sigma Ratio Constraint

GMMs are widely employed statistical tools, having thus a long history of use and study of their caveats. In particular, a relatively small concentration of data points around a value, due noise or instrumental error, can lure the fitting tool of use—in our case, the EM algorithm—in wrongly identifying said value as a mode. In the past, this possibility disabled the use of maximum likelihood methods in case of heteroscedastic splits, excluding all the mixtures in which different modes possess different deviation. The minimum-ratio constraint removes cases afflicted by this behavior and enables the use of maximum likelihood estimators [*Hathaway*, 1985].

As far back as in *Day* [1969], the use of maximum likelihood is recommended when it is known that the variances for the component densities are equal. However, *Hathaway* [1985] argues that the most important detail is not the equality of component variances, but the knowledge of their relative sizes, so that appropriate constraints of the form $\sigma_i = C_{ij}\sigma_j$ can be added, as shown by *Quandt and Ramsey* [1978].

As proposed by *Hathaway* [1985], we can use a filter based in a minimum threshold value for the ratio between the value of the standard deviation of the two modes. Exact knowledge is not required; instead, imprecise knowledge usually available can be imposed by using the set of linear inequality constraints $\sigma_i \geq \sigma_j/C_{ij}$, which can be written as

$$\min_{i,j} \frac{\sigma_i}{\sigma_j} \geq C \geq 0 \tag{14}$$

For reasonable choices of C, the constraints rule out the spurious local maximizers corresponding to the greatly differing standard deviations between the component densities [*Day*, 1969]. The value recommended in literature and used for this article is $C = 0.25$.

3.2.2. Weight Ratio Constraint

As argued in the case of the Sigma Ratio constraint, we can use our a priori knowledge of the studied phenomena in order to develop an additional constraint. Considering a reasonable assumption that a minimum percentage of the total data should be in each of the modes of a bimodal distribution, we can define an additional constraint, similar in formulation to the sigma ratio constraint:

$$\min_{i,j} \frac{\omega_i}{\omega_j} \geq C \geq 0 \tag{15}$$

In this case we consider that a reasonable value for C should be 0.1, meaning that each mode should contain at least 10% of the total sample points. This weight ratio constraint shares the same goal as the previous constraint; therefore, it is also a tool to avoid false mode identification. Even though this tool has the same structure and goal as the previously presented—thus causing certain overlap in their function—the general effectiveness of the classifying mechanism is nevertheless improved.

3.2.3. Ashman's *D*

Ashman et al. [1994] conducted sensitivity tests of the kernel mixture model-based maximum likelihood estimator and developed an additional independent test on bimodality. They defined a dimensionless separation of the means, originally tested for homoscedastic mixtures (i.e., when all modes have the same standard deviation), yet that can be reformulated for heteroscedastic mixtures (i.e., when modes have different standard deviations):

$$D = \frac{|\mu_1 - \mu_2|}{\sqrt{\left(\frac{\sigma_1^2+\sigma_2^2}{2}\right)}} \tag{16}$$

From the analytical results of *Ashman et al.* [1994] and *Everitt and Hand* [1981], concerning the detectability of bimodality, one of the simplest and most useful features is that such a distribution only shows two peaks if $D > 2$. If the GMM-EA method detects two modes but they are not separated enough ($D < 2$), then such a split is not meaningful. Therefore, here we consider adequate to use this alternative formulation as an additional test on bimodality.

3.3. Summary

After describing the log likelihood, EM algorithm, and the bimodality masks, our metric can be summarized as follows. First, after applying the masking criteria we obtain a binary classification: each grid cell is considered either potentially bimodal or not bimodal; counting the number of cells in each category leads to the results showed in Figure 3. Second, we display the difference between the log likelihood of the EM-adjusted GMM minus the log likelihood of the single Gaussian fit:

$$\Delta l(\lambda|x) = \log L_{\mathrm{GMM}}(\lambda|x) - \log L_{\mathrm{Gauss}}(\lambda|x) \tag{17}$$

This quantity, i.e., the difference between the log likelihood of the GMM and the log likelihood of the single Gaussian fit, when plotted as has been done in Figure 2, can give us an idea of how extreme or clear this bimodal behavior is, with lower values indicating either a behavior not clearly bimodal or simply not fitted

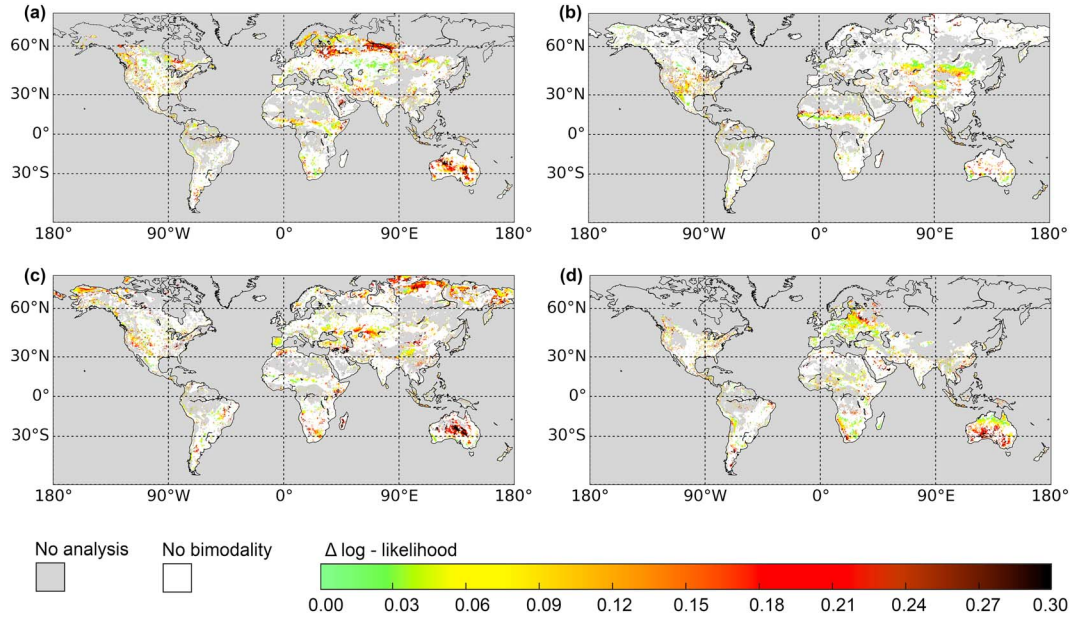

Figure 2. Global soil moisture log likelihood difference. Based on AMSR-E observations in four different periods: (a) northern hemisphere spring (week 11), (b) summer (week 24), (c) autumn (week 37), and (d) winter (week 50). The bimodal areas are colored, with higher values representing stronger bimodal behavior, while the blank areas are considered as nonbimodal and the gray areas are masked out for not meeting the inclusion criteria (see section 3.3).

to our assumptions and bigger values indicating a clear bimodal behavior. This method, in contrast with other possible but potentially more simple approaches, provides information about the physical properties of the modes which offer an insight to the surface conditions and climate characteristics in each area.

4. Results and Discussion

Areas of soil moisture bimodality for different seasons are illustrated in Figure 2, based on AMSR-E observations. The four AMSR-E timestamps are from weeks number 11, 24, 37, and 50, each of them taken as representative for the corresponding season. As mentioned above, it has been previously hypothesized that in regions where soil moisture is highly coupled to the atmosphere, wet or dry conditions may sustain themselves through positive land feedback causing periods of enhanced floods or droughts (respectively) [see, e.g., *D'Odorico and Porporato*, 2004]. While this would reflect in bimodal soil moisture distributions, the magnitude and sign of these feedback remain under debate [*Ek and Holtslag*, 2004; *Guillod et al.*, 2014; *Taylor et al.*, 2012]. Most of the bimodal areas found in Figure 2—such as the West and Midwest, central Australia, South Africa, or the Sahel—are in fact regions that have been reported as hot spots of land-atmosphere coupling, where soil moisture declines (increases) have generally been suggested to yield lower (higher) precipitation and higher (lower) air temperature [*Koster et al.*, 2004; *D'Odorico and Porporato*, 2004; *Miralles et al.*, 2012; *Tuttle and Salvucci*, 2016]. Areas of transitional climate regimes—i.e., where evaporation is typically sensitive to the variability of soil moisture [*Seneviratne et al.*, 2010]—are identified in *Koster et al.* [2004] and *Guo et al.* [2006] analyses and appear prominently in our results (Figure 2). Nonetheless, *Teuling et al.* [2005] indicated that the soil moisture bimodality in regions like Illinois [*D'Odorico and Porporato*, 2004] may not necessarily reflect land-atmospheric coupling but a combination of climate seasonality and nonlinear soil moisture responses. In fact, Figure 2 suggests that several well-known phenomena—such as the annual ground defrosting in Northern latitudes (Figure 2a) or the summer monsoons in Northern India and West Africa (Figure 2b)—may yield bimodal soil moisture distributions as well.

Figure 3a presents our results as the percentage of land area (per latitudinal band) that experiences soil moisture bimodality. Processes that may be expected to cause bimodality appear reflected in these latitudinal profiles: the large bimodality at 45–60°N (Figures 3a and 3b for the moving window starting at week 24; from now on we will refer to as "week 24" in both text and figures) corresponds with the transitional regime between boreal forest and arid terrain in Asia, which experiences seasonal freeze-thaw processes; the peak at

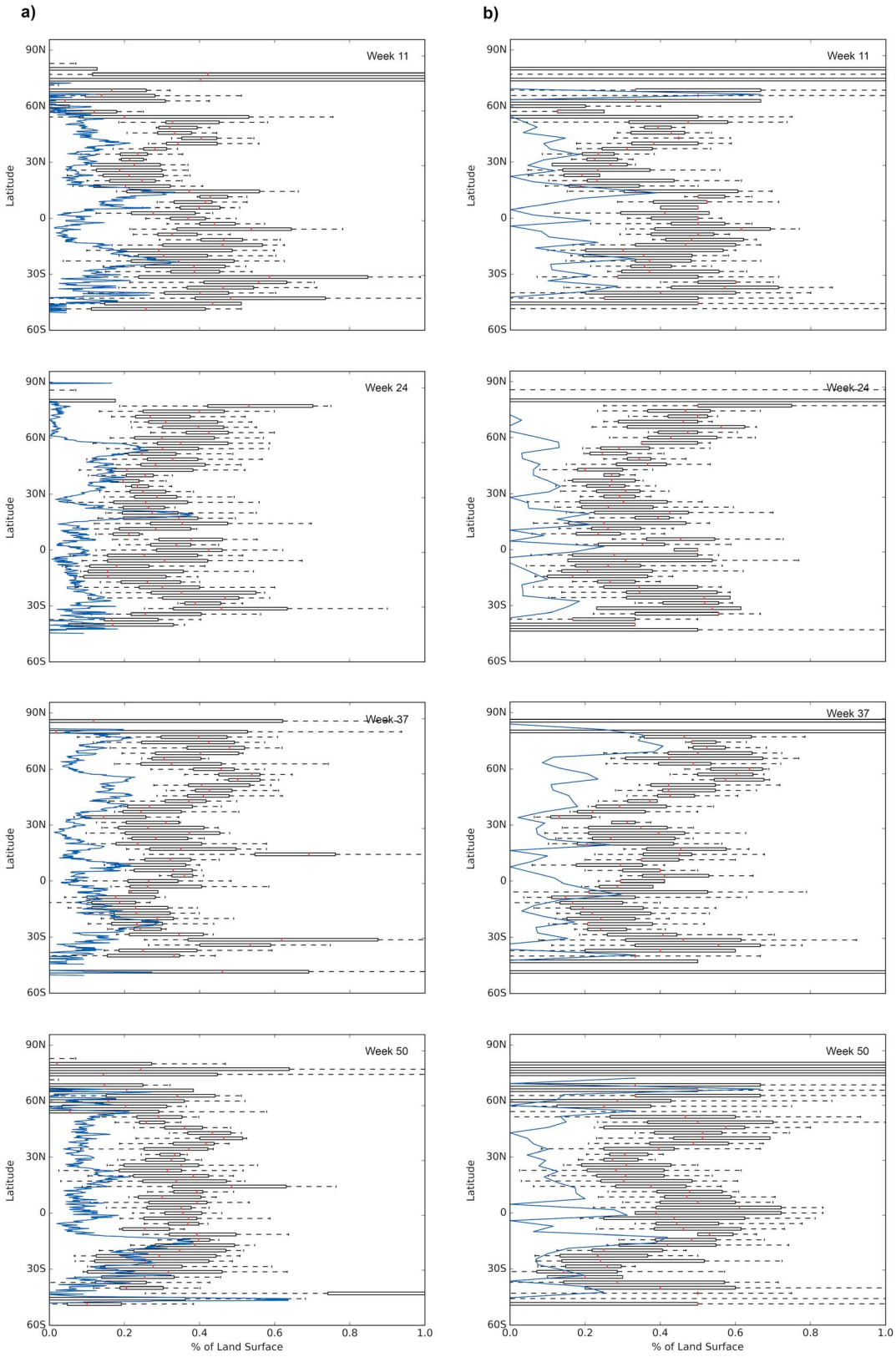

Figure 3. Latitudinal plots showing soil moisture bimodality in CMIP5 models and observations. Latitude is shown in the vertical and the percentage of land surface with bimodality in the horizontal. AMSR-E observations are represented in blue and the mean of the CMIP5 models in red. The boxplots represent the quartiles (0.25, 0.5, and 0.75 with the box) and data range (with the whiskers) from the CMIP5 models; thus, they provide an insight into the multimodel uncertainty. (a) Data sets used in their original resolution. (b) Data sets are resampled to a common 64 × 128 resolution.

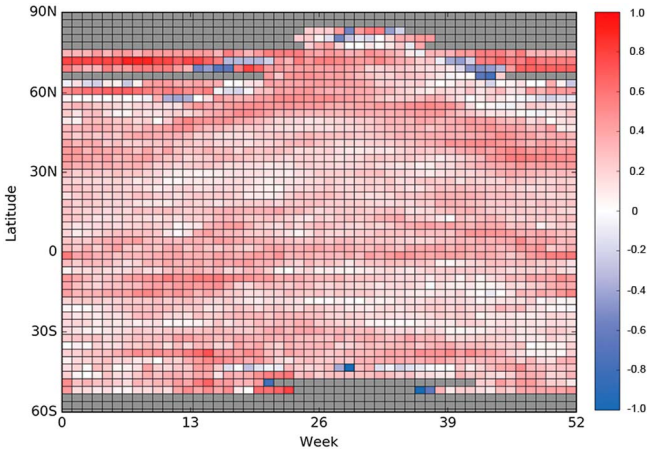

Figure 4. Year-round latitudinal plot color coding the difference between CMIP5 models and AMSR-E satellite observations. Latitude is shown in the vertical axis and week-of-the-year number on the horizontal axis. Each square depicts the integrated results of a latitudinal band for each week of the year. The normalized difference between the number of bimodal cells in models minus bimodal cells in the observational data set are color coded ([CMIP5 cells − AMSR-E cells]/analyzed cells), with red meaning a positive number, thus indicating a higher number of bimodal cells in a given latitude and time of the year.

15–20°N (Figures 3a and 3b for weeks 11, 24, and 37) is mostly due to the bimodality present in the Sahel and India during the monsoon seasons; and the high values around 30°S (Figures 3a and 3b for weeks 11, 37, and 50) correspond mostly to central Australia, a region of potentially high land-atmospheric coupling. CMIP5 models intermittently show a large data range in latitudinal bands (Figures 3a and 3b) associated with both monsoon and freeze-thaw processes suggesting certain degree of disagreement between models with regard of timing and location. A large range in percentage of bimodal cell is present in high latitudes (Figures 3a and 3b) due to the fact that at high latitudes the amount of grid cells available for analysis is lower and the area of each individual grid cell is smaller than in equatorial latitudes, turning the analysis results as shown in Figure 3 less tolerant to small errors.

Importantly, Figure 3a together with Figure 4 indicate that soil moisture bimodality is higher in all CMIP5 climate models than in satellite observations: GCMs tend to yield a higher bimodality, for all latitudes and all seasons. These higher values are typically more noticeable around the tropics and during the start of spring (Figures 3a and 3b for week 11 and Figure 4) and winter (Figures 3a and 3b for week 50 and Figure 4) and in high latitudes following the freeze-thaw cycle (Figure 4). While this may reflect a misrepresentation of soil moisture and land-atmospheric interactions in climate models, it could potentially be affected by the lower spatial resolution at which climate models operate (see Table S1). To test this hypothesis, we have replicated the analyses but based on a prior resampling of all data sets to a common 64×128 latitude-longitude resolution, the spatial resolution of the coarser GCMs (i.e., the Canadian Fourth Generation Atmospheric Global Climate Model, Beijing Climate Center Climate System Model, and Model for Interdisciplinary Research on Climate–Earth System Model). Figure 3b shows that both the latitudinal distribution and intensity of the bimodal response and its scatter and range within each latitudinal band are rather independent from the resolution at which data sets are analyzed. In fact, the differences between GCMs and observations become slightly more prominent when data sets are evaluated at coarser resolution.

Figure 4 shows the year-round evolution of the difference in bimodal cell count between models (as a multimodel average) and satellite observations. This figure highlights how the difference in soil moisture bimodality discussed in previous paragraphs varies during the whole year following the geographical evolution of land-atmosphere processes, showing a generally smooth evolution of the models-satellite discrepancy. The evolution of the freeze-thaw process is particularly clear, together with the monsoons. The blue areas indicating a higher satellite bimodal grid-cell count appear near the masked areas and in close proximity with the deep red areas suggesting a generalized timing discrepancy between CMIP5 models and AMSR-E regarding freeze-thaw in high latitudes.

Taylor et al. [2012] indicated a strong preference for positive soil moisture-precipitation feedback in current GCMs. This model behavior, favoring the likelihood of precipitation over wetter soils and disfavoring it under dry conditions, is a likely explanation for the higher values of soil moisture bimodality in GCM found in our analyses. This tendency to exaggerate the positive sign of this land-atmosphere feedback was also suggested by *Koster et al.* [2006] and *Mccrary and Randall* [2010] and potentially relates to errors in the representation of the diurnal cycle of precipitation and particularly of deep convection [*Guichard et al.*, 2004]. However, our bimodality diagnostic should be taken as an integrative measure of the representation of soil moisture-climate interactions, which incorporates a plethora of factors; aiming to identify a single process responsible for the discrepancies between GCMs and observations is therefore not in the scope of this analysis.

5. Conclusion

Soil moisture bimodality still remains by and large an elusive concept. In order to perform a global assessment of bimodality, several analytical steps have been followed. Our framework estimates soil moisture bimodality in regions and times in which global processes that are thought to be associated to bimodal distributions occur; this is the case of freeze-thaw processes or summer monsoons. In addition, CMIP5 models show a clearly higher values on bigger areas in which bimodality occurs. Even though models follow a common pattern, they strongly differ from the observation-based results, and this divergence does not respond to the higher resolution of the observations. A possible explanation for this behavior is that models tend to "lock-in" dry or wet conditions due to unrealistically positive soil moisture-precipitation feedback, a feature that has already been highlighted in previous studies. Our diagnostic of soil moisture bimodality appears therefore as an integrative tool to identify land-climate interactions and to benchmark their representation in climate models.

Acknowledgments

The authors acknowledge the World Climate Research Programme's Working Group on Coupled Modelling, which is responsible for CMIP, and we thank the climate modeling groups (listed in Table S1) for producing and making available their model output. For CMIP the U.S. Department of Energy's Program for Climate Model Diagnosis and Intercomparison provides coordinating support and led development of software infrastructure in partnership with the Global Organization for Earth System Science Portals. CMIP5 model data can be accessed from its data portal "http://cmip-pcmdi.llnl.gov/cmip5/data_portal.html". The authors also acknowledge the creators of the LPRM/AMSR-E/Aqua Daily L3 Surface Soil Moisture data set: the Vrije Universiteit Amsterdam and NASA GSFC and its publisher, the Goddard Earth Sciences Data and Information Services Center (GES DISC). LPRM AMSR-E data can be downloaded from ftp server "ftp://hydro1.sci.gsfc.nasa.gov/data/s4pa/WAOB/". L.U. Vilasa acknowledges the financial support from the Netherlands Organization for Scientific Research through NWO China Water/84200008/Land Atmos project. D. G. Miralles acknowledges support from the European Research Council (ERC) under grant agreement 715254 (DRY-2-DRY). A.J. Dolman acknowledges support from the program of the Netherlands Earth System Science Centre (NESSC), financially supported by the Ministry of Education, Culture and Science (OCW) (grant 024.002.001). The contribution of R.A.M. de Jeu was funded by the European Space Agency Climate Change Initiative for Soil Moisture (contract 4000104814/11/I-NB).

References

Albergel, C., G. Balsamo, P. De Rosnay, J. Muñoz-Sabater, and S. Boussetta (2012), A bare ground evaporation revision in the ECMWF land-surface scheme: Evaluation of its impact using ground soil moisture and satellite microwave data, *Hydrol. Earth Syst. Sci.*, *16*(10), 3607–3620, doi:10.5194/hess-16-3607-2012.

Ashman, K. A., C. M. Bird, and S. E. Zepf (1994), Detecting bimodality in astronomical datasets, *Astron. J.*, *108*, 2348–2361, doi:10.1086/117248.

Balsamo, G., et al (2012), ERA-Interim/land: A global land-surface reanalysis based on ERA-Interim meteorological forcing, ERA Report Series vol. 13, ECMWF, Reading.

Bartalis, Z., W. Wagner, V. Naeimi, S. Hasenauer, K. Scipal, H. Bonekamp, J. Figa, and C. Anderson (2007), Initial soil moisture retrievals from the METOP-A Advanced Scatterometer (ASCAT), *Geophys. Res. Lett.*, *34*, L20401, doi:10.1029/2007GL031088.

Bolten, J. D., W. T. Crow, X. Zhan, T. J. Jackson, and C. A. Reynolds (2010), Evaluating the utility of remotely sensed soil moisture retrievals for operational agricultural drought monitoring, *IEEE J. Sel. Top. Appl. Earth Obs. Remote Sens.*, *3*(1), 57–66, doi:10.1109/JSTARS.2009.2037163.

Collins, W. J., et al. (2011), Development and evaluation of an Earth-system model HadGEM2, *Geosci. Model Dev.*, *4*, 1051–1075, doi:10.5194/gmd-4-1051-2011.

Crow, W. T., and M. J. Van Den Berg (2010), An improved approach for estimating observation and model error parameters in soil moisture data assimilation, *Water Resour. Res.*, *46*, W12519, doi:10.1029/2010WR009402.

D'Odorico, P., and A. Porporato (2004), Preferential states in soil moisture and climate dynamics, *Proc. Natl. Acad. Sci. U.S.A.*, *101*(24), 8848–8851, doi:10.1073/pnas.0401428101.

D'Odorico, P. D., L. Ridolfi, and A. Porporato (2000), The impact of climate fluctuations, *Water Resour. Res.*, *36*(8), 2209–2219, doi:10.1029/2000WR900103.

Daly, E., Y. Zinger, A. Deletic, and T. D. Fletcher (2009), A possible mechanism for soil moisture bimodality in humid-land environments, *Geophys. Res. Lett.*, *36*, L07402, doi:10.1029/2008GL036933.

Day, N. E. (1969), Estimating the components of a mixture of normal distributions, *Biometrika*, *56*(3), 463–474, doi:10.1093/biomet/56.3.463.

Douville, H., S. Conil, S. Tyteca, and A. Voldoire (2006), Soil moisture memory and West African monsoon predictability: Artefact or reality?, *Clim. Dyn.*, doi:10.1007/s00382-006-0207-8.

Ek, M. B., and A. A. M. Holtslag (2004), Influence of soil moisture on boundary layer cloud development, *J. Hydrometeorol.*, *5*(1), 86–99, doi:10.1175/1525-7541.

Entekhabi, D., et al. (1999), An agenda for land surface hydrology research and a call for the second international hydrological decade, *Bull. Am. Meteorol. Soc.*, *80*(10), 2043–2058.

Essery, R., and D. B. Clark (2003), Developments in the MOSES 2 land-surface model for PILPS 2e, *Global Planet. Change*, *38*(1–2), 161–164, doi:10.1016/S0921-8181(03)00026-2.

Everitt, B. S., and D. J. Hand (1981), Mixtures of discrete distributions, in *Finite Mixture Distributions*, pp. 89–105, Springer Netherlands, Dordrecht, doi:10.1007/978-94-009-5897-5_4

Gates, W. L. (1992), AMIP: The Atmospheric Model Intercomparison Project, *Bull. Am. Meteorol. Soc.*, *73*(12), 1962–1970, doi:10.1175/1520-0477.

Guichard, F., et al. (2004), Modelling the diurnal cycle of deep precipitating convection over land with cloud-resolving models and single-column models, *Q. J. R. Meteorol. Soc.*, *130*(604), 3139–3172, doi:10.1256/qj.03.145.

Guillod, B. P., et al. (2014), Land-surface controls on afternoon precipitation diagnosed from observational data: Uncertainties and confounding factors, *Atmos. Chem. Phys.*, *14*(16), 8343–8367, doi:10.5194/acp-14-8343-2014.

Guo, Z., et al. (2006), GLACE: The global land–atmosphere coupling experiment. Part II: Analysis, *J. Hydrometeor.*, *7*, 611–625, doi:10.1175/JHM511.1.

Gupta, M. R., and Y. Chen (2010), Theory and use of the EM algorithm, *Found. Trends Signal Process.*, *4*(3), 223–296, doi:10.1561/2000000034.
Hathaway, R. J. (1985), A constrained formulation of maximum-likelihood estimation for normal mixture distributions, *Ann. Stat.*, *13*(2), 795–800, doi:10.1214/aos/1176349557.
Hirai, M., T. Sakashita, H. Kitagawa, and T. Tsuyuki (2007), Development and validation of a new land surface model for JMA's operational global model using the CEOP observation dataset, *J. Meteorol. Soc. Japan*, *85*, 1–24, doi:10.2151/jmsj.85A.1.
Hirschi, M., S. I. Seneviratne, V. Alexandrov, F. Boberg, C. Boroneant, O. B. Christensen, H. Formayer, B. Orlowsky, and P. Stepanek (2011), Observational evidence for soil-moisture impact on hot extremes in southeastern Europe, *Nat. Geosci.*, *4*(1), 17–21, doi:10.1038/ngeo1032.
Kerr, Y. H., et al. (2012), The SMOS Soil Moisture Retrieval Algorithm, *IEEE Trans. Geosci. Remote Sens.*, *50*(5), 1384–1403, doi:10.1109/TGRS.2012.2184548.
Koster, R. D., et al. (2004), Regions of strong coupling between soil moisture and precipitation, *Science*, *305*, 1138–1140, doi:10.1126/science.1100217.
Koster, R. D., et al. (2006), GLACE: The Global Land-Atmosphere Coupling Experiment. Part I: Overview, *J. Hydrometeorol.*, *7*, 590–610, doi:10.1175/JHM511.1.
Mccrary, R. R., and D. A. Randall (2010), Great plains drought in simulations of the twentieth century, *J. Clim.*, *23*(8), 2178–2196, doi:10.1175/2009JCLI3061.1.
Miralles, D. G., T. R. H. Holmes, R. A. M. De Jeu, J. H. Gash, A. G. C. A. Meesters, and A. J. Dolman (2011), Global land-surface evaporation estimated from satellite-based observations, *Hydrol. Earth Syst. Sci.*, *15*(2), 453–469, doi:10.5194/hess-15-453-2011.
Miralles, D. G., M. J. van den Berg, A. J. Teuling, and R. A. M. de Jeu (2012), Soil moisture-temperature coupling: A multiscale observational analysis, *Geophys. Res. Lett.*, *39*, L21707, doi:10.1029/2012GL053703.
Miralles, D. G., A. J. Teuling, and C. C. Van Heerwaarden (2014), Mega-heatwave temperatures due to combined soil desiccation and atmospheric heat accumulation, *Nat. Geosci.*, *7*(5), 345–349, doi:10.1038/ngeo2141.
Mizuta, R., H. Yoshimura, H. Endo, T. Ose, K. Kamiguchi, M. Hosaka, M. Sugi, S. Yukimoto, S. Kusunoki, and A. Kitoh (2012), Climate simulations using MRI-AGCM3.2 with 20-km grid, *J. Meteorol. Soc. Japan*, *90*, 233–258, doi:10.2151/jmsj.2012-A12.
Mueller, B., and S. I. Seneviratne (2012), Hot days induced by precipitation deficits at the global scale, *Proc. Natl. Acad. Sci. U.S.A.*, *109*(31), 12398–12403, doi:10.1073/pnas.1204330109.
Noilhan, J., and J. F. Mahfouf (1996), The ISBA land surface parameterisation scheme, *Global Planet. Change*, *13*(1–4), 145–159, doi:10.1016/0921-8181(95)00043-7.
Oleson, K., G. B. Bonan, S. Levis, P. Thornton, M. Vertenstein, and Z. Yang (2004), Technical description of the community land model (CLM), *NCAR Technical Note*, *461*, 1–174, doi:10.5065/D6N877R0.
Owe, M., R. de Jeu, and T. Holmes (2008), Multisensor historical climatology of satellite-derived global land surface moisture, *J. Geophys. Res.*, *113*, F01002, doi:10.1029/2007JF000769.
Parinussa, R. M., A. G. C. A. Meesters, Y. Y. Liu, W. Dorigo, W. Wagner, and R. A. M. De Jeu (2011), Error estimates for near-real-time satellite soil moisture as derived from the land parameter retrieval model, *IEEE Geosci. Remote Sens. Lett.*, *8*(4), 779–783, doi:10.1109/LGRS.2011.2114872.
Poveda, G., A. Jaramillo, M. M. Gil, N. Quiceno, and R. I. Mantilla (2001), Seasonality in ENSO-related precipitation, river discharges, soil moisture, and vegetation index in Colombia, *Water Resour. Res.*, *37*(8), 2169–2178, doi:10.1029/2000WR900395.
Quandt, R. E., and J. B. Ramsey (1978), Estimating mixtures of normal distributions and switching regressions, *J. Am. Stat. Assoc.*, *73*(364), 730–738, doi:10.1198/016214507000000932.
Reichle, R. H., R. D. Koster, G. J. M. De Lannoy, B. A. Forman, Q. Liu, S. P. P. Mahanama, and A. Toure (2011), Assessment and enhancement of MERRA land surface hydrology estimates, *J. Clim.*, *24*(24), 6322–6338, doi:10.1175/JCLI-D-10-05033.1.
Rosenzweig, C., and F. Abramopoulos (1997), Land-surface model development for the GISS GCM, *J. Clim.*, *10*(8), 2040–2054, doi:10.1175/1520-0442.
Schmidt, G. A., et al. (2006), Present-day atmospheric simulations using GISS ModelE: Comparison to in situ, satellite, and reanalysis data, *J. Clim.*, *19*(1), 153–192, doi:10.1175/JCLI3612.1.
Scipal, K., T. Holmes, R. De Jeu, V. Naeimi, and W. Wagner (2008), A possible solution for the problem of estimating the error structure of global soil moisture data sets, *Geophys. Res. Lett.*, *35*, L24403, doi:10.1029/2008GL035599.
Seneviratne, S. I., T. Corti, E. L. Davin, M. Hirschi, E. B. Jaeger, I. Lehner, B. Orlowsky, and A. J. Teuling (2010), Investigating soil moisture-climate interactions in a changing climate: A review, *Earth Sci. Rev.*, *99*, 125–161, doi:10.1016/j.earscirev.2010.02.004.
Takata, K., S. Emori, and T. Watanabe (2003), Development of the minimal advanced treatments of surface interaction and runoff, *Global Planet. Change*, *38*(1–2), 209–222, doi:10.1016/S0921-8181(03)00030-4.
Taylor, C. M., R. A. M. de Jeu, F. Guichard, P. P. Harris, and W. A. Dorigo (2012), Afternoon rain more likely over drier soils, *Nature*, *489*(7416), 423–426, doi:10.1038/nature11377.
Taylor, K. E., R. J. Stouffer, and G. A. Meehl (2011), An overview of the CMIP5 and the experiment design, *Bull. Amer. Meteor. Soc.*, *93*, 485–498, doi:10.1175/BAMS-D-11-00094.1.
Teuling, A. J., et al. (2010), Contrasting response of European forest and grassland energy exchange to heatwaves, *Nat. Geosci.*, *3*(10), 722–727, doi:10.1038/ngeo950.
Teuling, A. J., R. Uijlenhoet, and P. A. Troch (2005), On bimodality in warm season soil moisture observations, *Geophys. Res. Lett.*, *32*, L13402, doi:10.1029/2005GL023223.
Tuttle, S., and G. Salvucci (2016), Empirical evidence of contrasting soil moisture–precipitation feedbacks across the United States, *Atmos. Sci. Lett.*, *352*(6287), 825–828, doi:10.1126/science.aaa7185.
van den Hurk, B., F. Doblas-Reyes, G. Balsamo, R. D. Koster, S. I. Seneviratne, and H. Camargo (2012), Soil moisture effects on seasonal temperature and precipitation forecast scores in Europe, *Clim. Dyn.*, *38*(1–2), 349–362, doi:10.1007/s00382-010-0956-2.
Verseghy, D. L. (2000), The Canadian land surface scheme (CLASS): Its history and future, *Atmos. Ocean*, *38*(1), 1–13, doi:10.1080/07055900.2000.9649637.
Voldoire, A., et al. (2013), The CNRM-CM5.1 global climate model: Description and basic evaluation, *Clim. Dyn.*, *40*(9–10), 2091–2121, doi:10.1007/s00382-011-1259-y.
Volodin, E. M., and V. N. Lykosov (1998), Parametrization of heat and moisture transfer in the soil-vegetation system for use in atmospheric general circulation models: 2. Numerical experiments in climate modeling, *Izv. Atmos. Oceanic Phys.*, *34*(5), 622–633.
Volodin, E. M., N. A. Dianskii, and A. V. Gusev (2010), Simulating present-day climate with the INMCM4.0 coupled model of the atmospheric and oceanic general circulations, *Izv. Atmos. Oceanic Phys.*, *46*(4), 414–431, doi:10.1134/S000143381004002X.
von Salzen, K., et al. (2013), The Canadian fourth generation atmospheric global climate model (CanAM4). Part I: Representation of physical processes, *Atmos. Ocean*, *51*(1), 104–125, doi:10.1080/07055900.2012.755610.

Watanabe, S., et al. (2011), MIROC-ESM: Model description and basic results of CMIP5-20c3m experiments, *Geosci. Model Dev. Discuss.*, *4*(2), 1063–1128, doi:10.5194/gmdd-4-1063-2011.

Wu, T., R. Yu, F. Zhang, Z. Wang, M. Dong, L. Wang, X. Jin, D. Chen, and L. Li (2010), The Beijing Climate Center atmospheric general circulation model: Description and its performance for the present-day climate, *Clim. Dyn.*, *34*(1), 123–147, doi:10.1007/s00382-008-0487-2.

Yukimoto, S., et al. (2012), A new global climate model of the Meteorological Research Institute: MRI-CGCM3—Model description and basic performance, *J. Meteorol. Soc. Japan*, *90A*, 23–64, doi:10.2151/jmsj.2012-A02.